Soft Matter

PAPER

View Article Online
View Journal | View Issue

Cite this: *Soft Matter*, 2025, 21, 2548

Quantitative rationalization of the unexpectedly moderate water wettability of poly(vinyl alcohol) surfaces: thermodynamic evaluation and prediction of surface hydrogen bonding†

Zhuohuan Guo, Zhuoyuan Ma* and Dayang Wang *

Received 24th December 2024,
Accepted 24th February 2025

DOI: 10.1039/d4sm01524j

rsc.li/soft-matter-journal

In this work, a series of poly(vinyl alcohol) (PVA) films with defined but varied water wettability was prepared by curing as-prepared PVA films at systematically adjusted temperatures. The polar components of surface energy ($\gamma^{s,p}$) of the resulting PVA films were calculated and correlated with the molecular configurations of their surface OH groups—free OH (OH_f), *trans*-hydrogen bonded OH (OH_t), and *gauche*-hydrogen bonded OH groups (OH_g)—with the aid of attenuated total reflectance Fourier transform infrared spectroscopy. By decomposing the $\gamma^{s,p}$ values of the PVA films as a sum of the contributions from OH_f, OH_t, and OH_g groups, the intrinsic $\gamma^{s,p}$ components of $OH_t\left(\gamma_t^{s,p*}\right)$ and $OH_g\left(\gamma_g^{s,p*}\right)$ were calculated to be 8.0 mN m^{-1} and 9.8 mN m^{-1}, respectively, which were substantially smaller than that of $OH_f\left(\gamma_f^{s,p*} = 50\ \text{mN m}^{-1}\right)$. This provided a thermodynamic foundation not only to rationalize the unexpectedly moderated surface hydrophilicity of PVA films but also to quantitatively predict the f_{HB} component of hydrogen-bonded OH groups on their surfaces according to their water wettability.

1 Introduction

Polymers are widely utilized as surface coating materials to bestow chemical diversity and biomimetic potential onto disparate solid surfaces.[1–7] In pursuit of eco-friendly industrial and household cleaning, hydrophilic polymers are increasingly favoured for crafting self-cleaning surfaces that are capable of cleaning themselves upon contact with water.[8–13] However, hydrophilic polymer surfaces struggle to fully unfold their built-in hydration potential in practical applications as a consequence of surface reconstruction (inward orientation) of the polar groups on their surfaces upon being exposed to the air environment and hydrogen bonding between surface polar groups (such as hydroxyl, amine, and carboxylic acid).[14–16] This significantly reduces the polar interaction components ($\gamma^{s,p}$) of surface energy and their contributions to the total surface energy (γ^s) of hydrophilic polymer coatings, resulting in moderate water wettability. To date, extensive experimental and theoretical efforts have been devoted to studying the impact of surface reconstruction on the water wettability of hydrophilic polymer surfaces.[17–19] However, there has been limited rational analysis of how hydrogen bonding between surface polar groups affects surface hydrophilicity. In this context, the present work aimed to develop a thermodynamic framework to quantitatively rationalize the impact of hydrogen bonding of surface polar groups on the water wettability of hydrophilic polymer thin films with the objective of describing their $\gamma^{s,p}$ as a sum of the intrinsic contributions from free polar groups $\left(\gamma_f^{s,p*}\right)$ and hydrogen-bonded ones $\left(\gamma_{HB}^{s,p*}\right)$ on their surfaces.

Poly(vinyl alcohol) (PVA) is known for its excellent water solubility and film-forming ability on both hydrophilic and hydrophobic substrates and biocompatibility.[20–22] Owing to its abundant OH side groups, PVA chains are capable of effectively forming hydrogen bonds, either with themselves (for instance, through repetitive freeze/thaw methods) or with other molecules, such as glutaraldehyde and tannic acid,[23–25] leading to the formation of excellent hydrogels that have been widely applied in many fields, such as biomedicine, soft electronics, seawater desalination, and oil/water separation.[26–32] However, due to this very hydrogen bonding, PVA thin films generally exhibit relatively large water contact angles in air ($\theta_{w/a}$ of 60°–72°).[33–36] Despite this, there are few studies on how this unexpectedly moderate water wettability is correlated with the hydrogen bonding configuration of surface OH groups. To address this issue, herein, model PVA thin films were prepared by casting from their aqueous solutions, whose $\theta_{w/a}$ were systematically altered by varying the drying temperatures. By meticulously differentiating the surface fractions

State Key Laboratory for Inorganic Synthesis and Preparative Chemistry, College of Chemistry, Jilin University, Changchun, 130012, China. E-mail: mzyjlu@163.com, wangdayang@jlu.edu.cn

† Electronic supplementary information (ESI) available. See DOI: https://doi.org/10.1039/d4sm01524j

of free OH groups (OH_f), *trans*-hydrogen bonded OH groups (OH_t), and *gauche*-hydrogen bonded OH groups (OH_g) – f_f, f_t and f_g – with the help of X-ray photoelectron spectroscopy (XPS) and attenuated total reflection Fourier transform infrared spectroscopy (ATR-FTIR), we managed to decompose the $\gamma^{s,p}$ of the model PVA thin films into the intrinsic contributions of the surface OH_f, OH_t, and OH_g groups – $\gamma_f^{s,p*}$, $\gamma_t^{s,p*}$, and $\gamma_g^{s,p*}$ – as described in eqn (1):

$$\gamma^{s,p} = f_f \cdot \gamma_f^{s,p*} + f_t \cdot \gamma_t^{s,p*} + f_g \cdot \gamma_g^{s,p*} \quad (1)$$

As such, the $\gamma_t^{s,p*}$ and $\gamma_g^{s,p*}$ were calculated to be 8.0 mN m^{-1} and 9.8 mN m^{-1}, respectively, which were substantially smaller than that of $\gamma_f^{s,p*}$ (50 mN m^{-1}) and served as the rationale behind the unexpected water wettability of the cast PVA thin films ($\theta_{w/a}$ of approx. 68°). The validity and generality of the resulting $\gamma_t^{s,p*}$ and $\gamma_g^{s,p*}$ were endorsed by their success in estimating the f_{HB} component of hydrogen-bonded OH groups on different types of PVA surfaces, according to the variant of eqn (1)–(13), in excellent agreement with spectroscopic analysis by means of ATR-FITR. In this scenario, therefore, the present work offers a thermodynamic framework to quantitatively rationalize and describe the impact of hydrogen bonding of surface polar groups on the water wettability of hydrophilic polymer surfaces.

2 Materials and methods

2.1 Materials

Three types of PVA with low, medium and high molecular weight were used to create thin films. PVA with a M_w of 13 000–23 000 and an alcoholysis degree of 98% (L-PVA) was purchased from Sigma-Aldrich Co., Ltd (Shanghai, China). PVA with a M_w of approx. 77 000 and alcoholysis degree of 98% (M-PVA) was obtained from China National Pharmaceutical Group Co., Ltd (Beijing, China). Finally, PVA with a M_w of 85 000–124 000 and alcoholysis degree of 98–99% (H-PVA) was purchased from Shanghai Chemical Co., Ltd (Shanghai, China). Hexadecane was purchased from Aladdin Bio-Chem Technology Co., Ltd (Shanghai, China). Water with a resistivity of 18 MΩ cm^{-1} was prepared using a Millipore Milli-Q system, and used in all experiments.

2.2 Methods

2.2.1 Preparation of the PVA surfaces. Aqueous PVA solution was prepared by dissolving a given amount of PVA powder in deionized water at 90 °C under magnetic stirring at 900 rpm for more than 2 h. After the PVA powder was completely dissolved, the resulting PVA solutions were cooled down to room temperature and filtered to remove any insoluble impurities, and their concentration was adjusted to be either 2 wt% or 7 wt%.

2.2.1.1 Preparation of the model L-PVA thin films. Model L-PVA thin films were prepared according to the protocol reported in the literature.[33] Then, 420 μL of the resulting aqueous solution of L-PVA (2 wt%) was dropwise cast into a thin film on a glass slide (2.5 × 2.5 cm^2), followed by 1 h drying at 20 °C, 50 °C, 80 °C, 110 °C, 140 °C, and 180 °C, respectively, and 24 h drying at room temperature in a desiccator. The drying duration was deliberately set to be 1 h in order to minimize the potential risk of heating-induced surface reconstruction, especially in high temperatures. The resulting model PVA films were denoted as $L\_PVA_2^T$, where the superscript "*T*" highlights the temperature of the first drying stage and the subscript "2" highlights the concentration of the PVA aqueous solutions used for casting.

Prior to the surface wetting test, the resulting $L\_PVA_2^T$ films were abraded using sandpaper to reveal the uniformity of their structural and chemical features across the bulk. The films were placed on 800 grit sandpaper and then pressed with a 100 g weight, which was pushed to move it along a ruler by 10 cm at a speed of 0.5 cm s^{-1}, then rotated 90°, and moved back in the same way. The above-mentioned process was defined as 1 abrasion cycle.

2.2.1.2 Preparation of H-PVA thin films. H-PVA thin films were prepared according to the protocol reported in the literature.[34] The resulting aqueous solution of H-PVA (2 wt%) with 420 μL was dropwise cast onto a glass slide (2.5 × 2.5 cm^2), followed by successively drying at 30 °C for 1 d, at 80 °C for 1 h, and at 40 °C under vacuum for 24 h. The resulting H-PVA films were denoted as $H\_PVA_2^{80}$.

2.2.1.3 Preparation of the L-PVA thin films. L-PVA thin films were prepared according to the protocol reported in the literature.[37] Then, 420 μL of the resulting aqueous solution of L-PVA (7 wt%) was dropwise cast onto a glass slide (2.5 × 2.5 cm^2), followed by 24 h drying under ambient conditions. The resulting L-PVA films were denoted as $L\_PVA_7^{RT}$.

2.2.1.4 Preparation of the dry PVA gel films. The PVA hydrogel was first prepared using the repeated freeze–thaw method.[38] Typically, 4 g of M-PVA powder was dissolved into a binary solvent consisting of 16 mL of DMSO and 4 mL of deionized water at 95 °C under magnetic stirring until a transparent and viscous solution was obtained. The resulting solution was then poured into a custom-made mold and subjected to 10 freeze–thaw cycles to form a hydrogel. After the hydrogel was demolded and thoroughly washed with deionized water to remove residual DMSO, it was thoroughly dried under ambient conditions for several days prior to surface wettability analysis. The resulting dried PVA gel films were denoted as $M\_PVA_G^{RT}$.

2.2.2 Surface wettability analysis. Contact angle measurement was implemented on a drop shape analyser – DSA100 system (Krüss GmbH, Germany) at ambient temperature. Prior to the contact angle test, the as-prepared PVA films were stored in a desiccator for 24 h at 25 °C under a relative humidity of 25–30% to ensure measurement consistency. The static $\theta_{w/a}$ values of the as-prepared PVA films were measured by placing a water droplet of 2 μL volume. The $\theta_{w/a}$ value of a given film surface was obtained as an average of three values was collected on different positions on the surface after the 2 μL droplets of water were placed on top and equilibrated for 10 s.

Calculations of γ^s, $\gamma^{s,p}$ and $\gamma^{s,d}$ were carried out on the basis of the Fowkes model for a surface wetted by water in air,[39] as

described in eqn (2):

$$\gamma_w(1+\cos\theta_{w/a}) = 2\sqrt{\gamma^{s,d}\cdot\gamma_w^d} + 2\sqrt{\gamma^{s,p}\cdot\gamma_w^p} \quad (2)$$

where γ_w is 72.8 mN m^{-1}, γ_w^d is 21.8 mN m^{-1} and γ_w^p is 51.0 mN m^{-1}.

2.3 Surface spectroscopic analysis

2.3.1 X-ray photoelectron spectroscopy (XPS). XPS was carried out on a Kratos Axis X-ray Ultra photoelectron spectrometer, in which monochromatic Al Kα (1486.6 eV) X-ray with power of 225 W was applied at an incidence angle of 90° to achieve a depth of detection of approx. 15 nm from the surface of the samples.

2.3.2 Attenuated total reflection Fourier transform infrared spectroscopy (ATR-FTIR). ATR-FTIR was carried out on a Nicolet Aratar 370 attenuated total reflection Fourier transform spectrometer, in which zinc selenide crystals were used as internal reflecting elements at an incidence angle of 45°, and the spectral data for the experimental part were all cumulative averages obtained from 64 scans at a resolution of 4 cm^{-1}.

2.3.3 Step profiler. The thicknesses of the L_PVA$_2^{20}$ and L_PVA$_2^{180}$ films were measured by step profiler (KLA, D500), with three independent measurements performed to ensure statistical reliability.

3 Results and discussion

3.1 The water wettability of the model L-PVA thin films

PVA is capable of forming uniform thin films on both hydrophilic and hydrophobic substrates by means of simple casting of their aqueous solution.[20] A key feature of the resulting PVA thin films is that the OH side groups of PVA tend to effectively and extensively form hydrogen bonds with each other.[40] As suggested in the literature,[41–43] on the other hand, the gyration radius (R_g) of the PVA chains in an aqueous solution and the distance between their OH groups can be regulated by temperature, thus enabling adjustment of the fraction of hydrogen-bonded OH (OH_{HB}) groups on the cast PVA thin films. To study the impact of hydrogen bonding of the surface OH groups on the water wettability on the PVA surfaces, here 6 different model surfaces (L_PVA$_2^T$) were prepared by casting the aqueous solution of L-PVA into thin films, followed by drying at 20 °C, 50 °C, 80 °C, 110 °C, 140 °C, and 180 °C, respectively, as described in 2.2.1.1. UV-vis spectroscopic analysis demonstrates the excellent transparency of the as-prepared L_PVA$_2^T$ thin films (Fig. 1a), and atomic force microscopic (AFM) imaging reveals their excellent surface smoothness with a root mean square (RMS) roughness in the range of 1.67 nm to 1.82 nm (Fig. 1b). The thicknesses of the L_PVA$_2^{20}$ and L_PVA$_2^{180}$ thin films were 7.0 μm and 7.3 μm by the step profiler, respectively. These results rule out the impact of the surface structural features of the L_PVA$_2^T$ thin films on their surface hydrophilicity. To ensure measurement consistency, the as-prepared L_PVA$_2^T$ thin films were subjected to 24 h incubation in a desiccator under

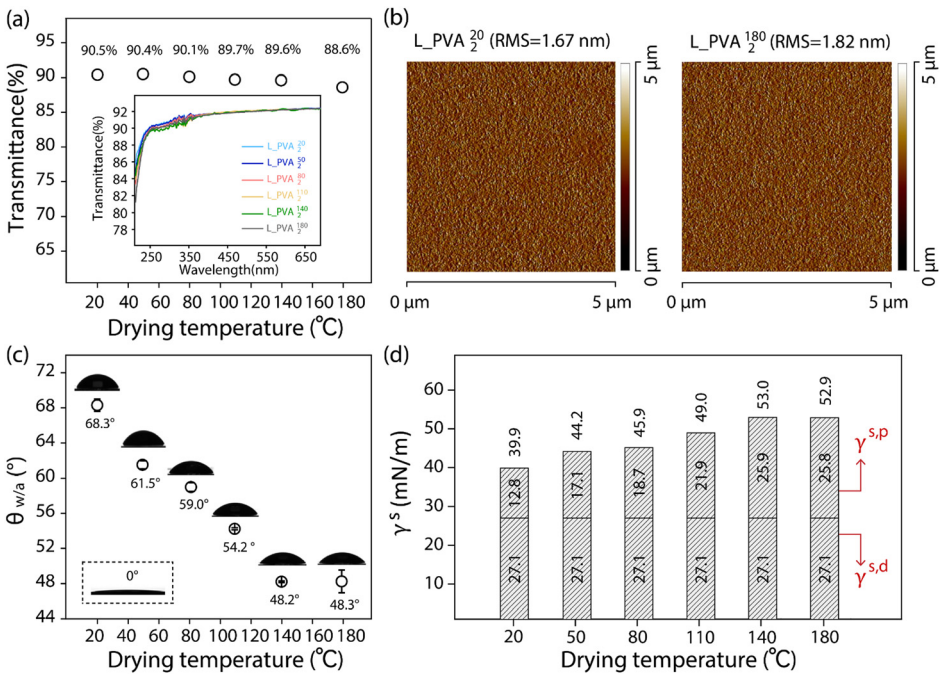

Fig. 1 (a) Plot of the transmittance values of the as-prepared L_PVA$_2^T$ thin films deposited on glass slides *versus* the drying temperature (*T*). The inset shows the corresponding UV-vis spectra in the wavelength range of 200–700 nm. (b) AFM images of the as-prepared L_PVA$_2^{20}$ and L_PVA$_2^{180}$ thin films, with the corresponding RMS values marked. (c) Plot of the $\theta_{w/a}$ values of the as-prepared L_PVA$_2^T$ thin films *versus* the drying temperature (*T*), with schematics of a 2 μL droplet of water placed on the corresponding L_PVA$_2^T$ thin films and a 2 μL hexadecane droplet placed on the L_PVA$_2^{20}$ thin films shown. (d) Histogram of the values of γ^s, $\gamma^{s,d}$ and $\gamma^{s,p}$ of the as-prepared L_PVA$_2^T$ thin films.

controlled conditions (25 °C, relative humidity 25–30%) prior to the contact angle test, although they showed negligible change in $\theta_{w/a}$ during storage under ambient conditions. Fig. 1c shows that the $\theta_{w/a}$ of the L_PVA$_2^T$ thin films decreases from 68.3° to 48.3° with the drying temperature increasing from 20 °C to 180 °C. The revealed moderate water wettability reflects that surface OH groups on the L_PVA$_2^T$ thin films tend to form hydrogen bonds not with water but with each other, which can be notably disrupted when the cast thin film is dried at elevated temperatures. However, a further increase in the temperature from 140 °C to 180 °C causes little change in $\theta_{w/a}$. This is because the negative impact of surface reconstruction becomes negligible when the cast PVA thin films are dried at such high temperature even for a short period of time. As shown in Fig. 1d, the pronounced negative impact of hydrogen bonding of the surface OH groups is endorsed by the unexpected small $\gamma^{s,p}$ values of the L_PVA$_2^T$ thin films – the $\gamma^{s,p}$ of the L_PVA$_2^{20}$ thin films being 12.8 mN m^{-1} – especially taking into account the $\gamma^{s,p}$ maximum theoretically expected for surface OH groups ($\gamma_f^{s,p*}$ of 50 mN m^{-1}).[17] The elevation of the drying temperature from 20 °C and 140 °C can drive the $\gamma^{s,p}$ of the resulting L_PVA$_2^T$ thin films by about 2 times due to disruption of the OH_{HB} groups into OH_f groups on their surfaces, yet the $\gamma^{s,p}$ of the L_PVA$_2^{140}$ thin film (25.8 mN m^{-1}) remains about 2 times smaller than the $\gamma_f^{s,p*}$ of the surface OH groups (50 mN m^{-1}). On the other hand, it is worth noting that the $\gamma^{s,d}$ of all as-prepared L_PVA$_2^T$ thin films is around 27.1 mN m^{-1}. As suggested in the literature,[17] this indicates that the resulting PVA thin films are composed of densely packed PVA chains, thus ensuring stable $\theta_{w/a}$ values.

3.2 The molecular configurations of surface OH groups on model L-PVA thin films

In order to gain a better understanding of the molecular configurations of OH groups on the as-prepared L_PVA$_2^T$ thin films, both XPS and ATR-FTIR spectroscopies were applied to characterize their surfaces. As shown in Fig. 2a–c, the L_PVA$_2^T$ thin films show three distinct C 1s bands centred at 284.6, 286.2, and 289.0 eV, corresponding to C–H, C–OH, and O–C═O groups, respectively. While the presence of the O–C═O group indicates incomplete alcoholysis of the L-PVA used, the profiles and portions of the C 1s bands of the L_PVA$_2^T$ thin films are hardly dependent on the drying temperature, which rules out the disparity in the chemical composition between the L_PVA$_2^T$ thin films and their impact on their surface hydrophilicity. Fig. 2d shows the ATR-FTIR spectra of the L_PVA$_2^T$ thin films, in which a prominent band centered at 3273 cm^{-1} is assigned to the stretching vibrations of the OH_{HB} groups of the PVA chains. Neither free OH side groups of the PVA chains (centred around 3600 cm^{-1}) nor those forming hydrogen bonds with water molecules (centred around 3460 cm^{-1}) are visible. It is worth noting that the vibrational band of the OH_{HB} groups of the L_PVA$_2^T$ thin films becomes weaker with increasing dry temperature, indicative of the temperature-induced disruption of the hydrogen bonds of the neighboring OH groups in the bulk environment and on the surface. Fig. 2e shows that the vibrational band of the OH_{HB} groups of the L_PVA$_2^{140}$ thin films and their water wettability remain largely unchanged after their surfaces are subjected to multiple cycles of abrasion *via* sandpaper, which is in line with the molecular configuration of the surface OH groups specifically revealed by means of sum frequency generation spectroscopy. These results highlight the uniformity of the molecular structures across the thin films. Thus, the hydrogen-bonding configurations of the OH side groups of the PVA chains, revealed in Fig. 2d, can reasonably represent the molecular configuration of the surface OH groups of the L_PVA$_2^T$ thin films. ATR-FITR spectroscopy is expected to sense thicker regions of about several μm in depth beneath their outermost surfaces,[44] though.

As reported in the literature,[45] the OH side groups of the PVA chains can adopt two distinct hydrogen-bonding configurations: *trans*- and *gauche*-configurations (Fig. 2f). For the L_PVA$_2^T$ thin films, there are three types of OH groups present on their surfaces: free OH group (OH_f), *trans*-hydrogen bonded OH groups (OH_t), and *gauche*-hydrogen bonded OH groups (OH_g). Fig. 2g shows that the ratio of the asymmetric C–C stretching vibration band (I_{Vasg}) of the PVA backbones to the corresponding symmetric stretching vibration band (I_{Vsst}) – I_{Vasg}/I_{Vsst} ratio – increases from 1.2 to 1.4 for the L_PVA$_2^T$ thin films with increasing drying temperature. This indicates that the temperature-induced disruption of hydrogen bonds of the OH groups for weak *gauche*-hydrogen bonds are expected to become more favourable than strong *trans*-hydrogen bonds at high temperatures.[44] Furthermore, Fig. 2h reveals that the vibrational bands of the OH_{HB} groups of the as-prepared L_PVA$_2^T$ thin films exhibit a notable dependence of their profile on the drying temperature. They can be readily decomposed into two bands centered at 3222 cm^{-1} and 3356 cm^{-1} with the assistance of Gaussian curve fitting, which can be assigned to strong *trans*- and weak *gauche*-hydrogen bonding configurations of the OH groups of PVA chains, respectively.[46,47] It is clear that with the drying temperature increasing to above 140 °C, the vibrational band of OH_t is more significantly reduced than that of OH_g. This reflects the fact that *gauche*-hydrogen bonding is weaker than *trans*-hydrogen bonding.

On the basis of the vibrational band deconvolution of the OH_{HB} groups from the resulting L_PVA$_2^T$ thin films, as shown in Fig. 2h, the fractions of OH_t and OH_g – marked as ϕ_i^T where i represents t or g – among their hydrogen-bonded OH groups can be estimated according to the following equations:

$$A_i^T = d \cdot c_i^T \cdot \int_0^{+\infty} \varepsilon_i(v) dv \quad (3)$$

$$\phi_i^T = c_i^T / c_{HB}^T = A_i^T / A_{HB}^T \quad (4)$$

$$\phi_t^T + \phi_g^T = 1 \quad (5)$$

where A_i^T represents the integrated intensity of the corresponding vibrational bands of OH_t or OH_g, c_i^T is the concentration of OH_t or OH_g groups (per volume for the entire films or per area for the film surface) and ϕ_i^T is their corresponding fraction. In eqn (3), d is the detection pathway length and $\varepsilon_i(v)$ is the wavenumber (v)-dependent absorption coefficient of PVA. In eqn (4), A_{HB}^T is the integrated intensity of the vibrational bands of the OH_{HB} groups and c_{HB}^T is their concentration.

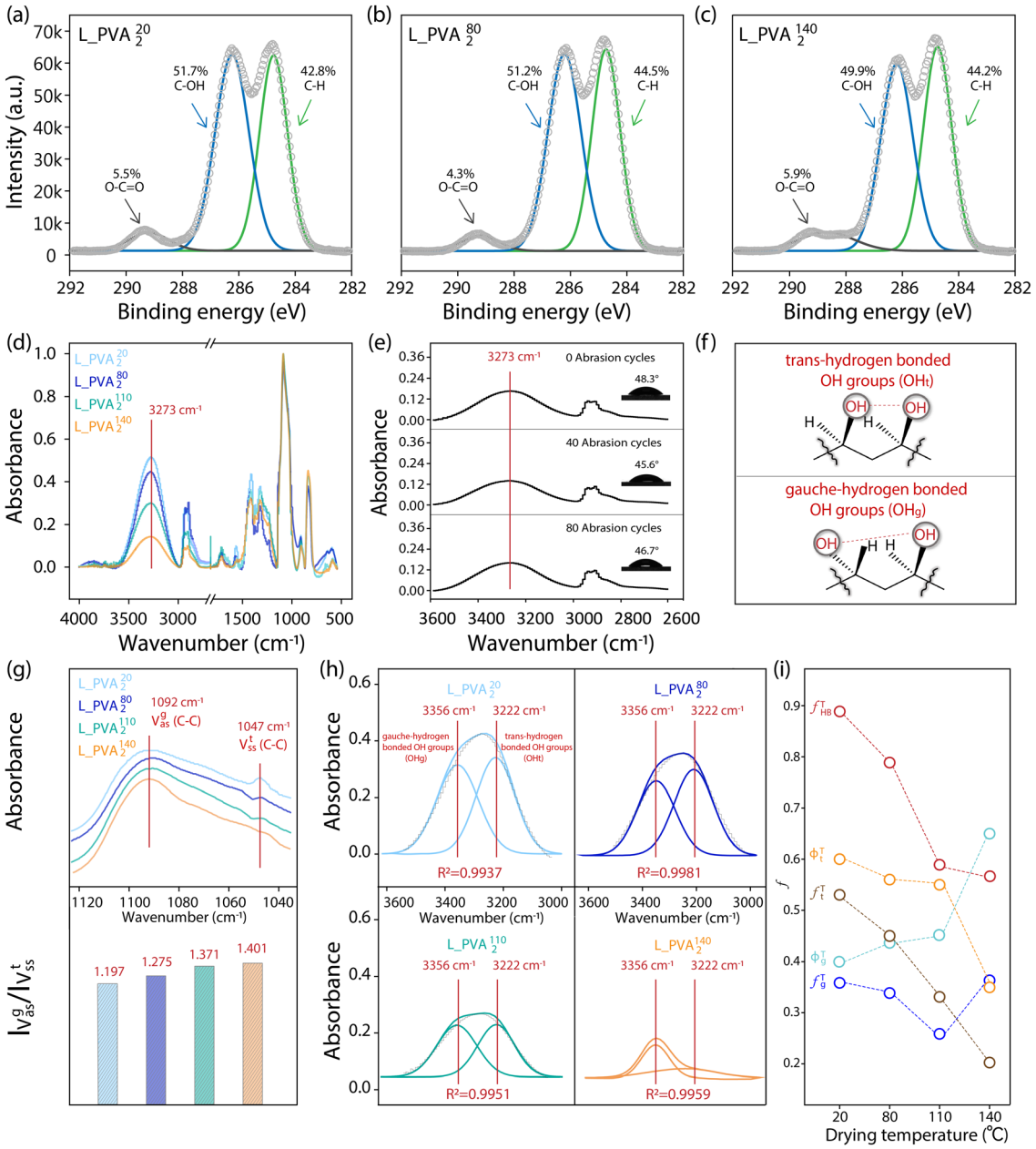

Fig. 2 (a)–(c) High-resolution XPS spectra of the C 1s signals of L_PVA$_2^{20}$ (a), L_PVA$_2^{80}$ (b), and L_PVA$_2^{140}$ thin films (c). (d) ATR-FTIR spectra of the L_PVA$_2^{20}$, L_PVA$_2^{80}$, L_PVA$_2^{110}$, and L_PVA$_2^{140}$ thin films in the range of 4000–400 cm^{-1}. (e) ATR-FTIR spectra of the as-prepared L_PVA$_2^{140}$ thin films after their surfaces were subjected to 0, 40 and 80 cycles of abrasion, with schematics of the 2 μL water droplets placed on the corresponding surfaces shown in the inset. (f) Schematic depiction of the *trans*- and *gauche*-hydrogen bonding configurations of the OH groups of the PVA chains. (g) ATR-FTIR spectra of the hydrocarbon backbones of the PVA chains of the as-prepared L_PVA$_2^T$ thin films in the range of 1130–1030 cm^{-1}, with their corresponding I_{Vasg}/I_{Vsst} values. (h) ATR-FTIR spectra of the OH side groups of the PVA chains of as-prepared L_PVA$_2^T$ thin films in the range of 3600–3000 cm^{-1}, with the spectra deconvoluted into the vibrational bands of the OH$_t$ and OH$_g$ groups using Gaussian curve fitting. (i) Plots of the calculated f_{HB}^T, f_t^T, ϕ_t^T, f_g^T and ϕ_g^T values of the as-prepared L_PVA$_2^T$ thin films *versus* the drying temperature (T).

Accordingly, the fractions of the OH$_f$ and OH$_{HB}$ groups, as well as the latter components OH$_t$ and OH$_g$ – marked as f_i^T where i represents f, HB, t or g – can be described by the following equations:

$$f_{HB}^T = c_{HB}^T/c_{OH}^T = A_{HB}^T/A_{OH}^T \quad (6)$$

$$f_f^T + f_{HB}^T = f_f^T + f_t^T + f_g^T = 1 \quad (7)$$

$$f_{t(g)}^T = \phi_{t(g)}^T \cdot f_{HB}^T \quad (8)$$

where A_{OH}^T is the integrated intensity of the vibrational bands of the total OH groups and c_{OH}^T is their concentration. Since the vibrational band of the OH$_f$ groups is hardly visible for the L_PVA$_2^T$ thin films, we were not able to estimate the values of A_{OH}^T (or c_{OH}^T) and in turn, those of f_f^T and f_{HB}^T from their ATR-FITR spectra (Fig. 2h). After, the vibrational band of the

Table 1 Summary of the values of f_f^T, f_{HB}^T, A_i^T, ϕ_i^T, and f_i^T of the as-prepared L_PVA$_2^T$ thin films and their corresponding $\gamma^{s,p}$ and $\gamma_{HB(T)}^{s,p}$ values, where i represents t and g

L_PVA$_2^T$	f_f^T	f_{HB}^T	A_t^T	ϕ_t^T	f_t^T	A_g^T	ϕ_g^T	f_g^T	$\gamma^{s,p}$ (mN m^{-1})	$\gamma_{HB(T)}^{s,p}$ (mN m^{-1})
L_PVA$_2^{20}$	0.11	0.89	59.5	0.60	0.53	41.7	0.40	0.36	12.8	7.3
L_PVA$_2^{80}$	0.21	0.79	50.5	0.56	0.45	39.6	0.44	0.34	18.7	8.2
L_PVA$_2^{110}$	0.41	0.59	37.1	0.55	0.33	30.0	0.45	0.26	21.9	1.4
L_PVA$_2^{140}$	0.44	0.56	22.7	0.35	0.20	42.5	0.65	0.36	25.9	3.9

OH_{HB} groups from the resulting L_PVA$_2^T$ thin films are deconvolved *via* Gaussian curve fitting with coefficient of determination (R^2) above 0.99. To circumvent this issue, here are the values of f_f^T and f_{HB}^T, which were theoretically estimated according to molecular dynamics simulation data reported in the literature.[48] For a solid surface consisting of 30 PVA chains with 150 OH groups, the number of hydrogen bonds formed between these OH groups were found to be 266 instead of 300, the theoretical maximum. Bearing that in mind, the f_{HB}^{20} of the resulting L_PVA$_2^{20}$ thin films is assumed to be 0.89 (266/300). Thus, the f_{HB}^T of the other L_PVA$_2^T$ thin films are estimated according to eqn (9):

$$f_{HB}^T = f_{HB}^{20} \cdot (A_{HB}^T / A_{HB}^{20}) \quad (9)$$

The resulting f_{HB}^T values can be used to calculate the corresponding f_f^T values according to eqn (7). By combining eqn (4), (8) and (9) into eqn (10):

$$f_{t(g)}^T = f_{HB}^{20} \cdot (A_i^T / A_{HB}^{20}) \quad (10)$$

The f_t^T and f_g^T of the L_PVA$_2^T$ thin films can be readily derived, listed in Table 1, from the A_{OH}^T values measured from the vibrational band of the OH_{HB} groups and their A_t^T and A_g^T components. With the drying temperature increasing, as shown in Fig. 2i, the f_{HB}^T and f_t^T of the resulting L_PVA$_2^T$ thin films notably decrease and yet their f_g^T remains hardly changed, which offers a quantitative testimony not only to the temperature-induced disruption of OH_{HB} groups, but also to the weak *gauche*-hydrogen bonding configurations being more favourable than the strong *trans*-hydrogen bonding configurations at high temperatures.

3.3 Quantitative differentiation of the contributions of hydrogen-bonded OH groups to the surface energy polar components of the model L-PVA thin films

As mentioned above, the molecular configurations of the OH_{HB} groups of the as-prepared L_PVA$_2^T$ thin films, revealed by means of ATR-FITR spectroscopic analysis, are expected not only in the bulk phase, but also on the surface thanks to the structural and chemical uniformity across the films. With that in mind, the $\gamma^{s,p}$ values of the L_PVA$_2^T$ thin films, marked as $\gamma_{(T)}^{s,p}$ to specify the drying temperature and summarized in Fig. 1d, are plotted *versus* their f_{HB}^T, f_t^T, and f_g^T values, which reveals that the increase in $\gamma^{s,p}$ is a reflection of more OH_{HB} groups being broken into OH_f groups with the increasing drying temperature (Fig. 3a). The contribution of OH_{HB} groups to the $\gamma_{(T)}^{s,p}$ of the L_PVA$_2^T$ thin films, specifically marked as $\gamma_{HB(T)}^{s,p}$ can be readily calculated according to eqn (11):

$$\gamma_{(T)}^{s,p} = (1 - f_{HB}^T) \cdot \gamma_f^{s,p*} + \gamma_{HB(T)}^{s,p} \quad (11)$$

The L_PVA$_2^T$ thin films exhibit fairly small $\gamma_{HB(T)}^{s,p}$ values in the range of 1.4–8.2 mN m^{-1} (listed in Table 1), which show random correlations with either the f_{HB}^T (or f_f^T) values or their components, f_t^T (or ϕ_t^T) and f_g^T (or ϕ_g^T) (Fig. 3b). By assuming that surface OH_t and OH_g groups independently contribute to surface energy, $\gamma_{HB(T)}^{s,p}$ can be decomposed into the intrinsic contributions of OH_t and OH_g groups – $\gamma_t^{s,p*}$ and $\gamma_g^{s,p*}$ – according to eqn (12):

$$\gamma_{HB(T)}^{s,p} = f_t^T \cdot \gamma_t^{s,p*} + f_g^T \cdot \gamma_g^{s,p*} = f_{HB}^T \left(\varphi_t^T \cdot \gamma_t^{s,p*} + \varphi_g^T \cdot \gamma_g^{s,p*} \right) \quad (12)$$

In order to implement the computational determination of parameters $\gamma_t^{s,p*}$ and $\gamma_g^{s,p*}$, we substituted $\gamma_f^{s,p*}$ of 50 mN m^{-1} into eqn (1) and transformed it into eqn (13):

$$(\gamma_t^{s,p*} - 50) \cdot f_t + \left(\gamma_g^{s,p*} - 50 \right) \cdot f_g - (\gamma^{s,p} - 50) = 0 \quad (13)$$

Thus, eqn (13) is a first-order three-variable equation in the form of $Ax_1 + Bx_2 - y = 0$, where f_t, f_g and $(\gamma^{s,p} - 50)$ are the three variables of x_1, x_1 and y, respectively, and $(\gamma_t^{s,p*} - 50)$ and $\left(\gamma_g^{s,p*} - 50 \right)$ are the A and B constants, respectively. By utilizing all four sets of data listed in Table 1, eqn (13) can be well fitted according to a multiple linear regression model with R^2 of 0.9924, yielding $\gamma_t^{s,p*}$ of 8.0 mN m^{-1} with a standard deviation (SD) of 0.67 mN m^{-1} and 95% confidence interval (CI) of 7.5 ± 1.5 mN m^{-1} and $\gamma_g^{s,p*}$ of 9.8 mN m^{-1} with SD of 0.53 mN m^{-1} and CI of 9.1 ± 1.2 mN m^{-1}. For the as-prepared L_PVA$_2^T$ thin films, their $\gamma^{s,p}$ can thus be written as a sum of the intrinsic contributions of the surface OH_f, OH_t, and OH_g groups – $\gamma_f^{s,p*}$, $\gamma_t^{s,p*}$, and $\gamma_g^{s,p*}$ – according to eqn (1) (Fig. 3c). In the *trans* configuration, the relative orientation of two adjacent carbon atoms within the molecule is linear, resulting in a spatial arrangement that is both more stable and symmetrical. This configuration typically corresponds to a lower energy state. Conversely, in the *gauche* configuration, the relative orientation angle between the adjacent carbon atoms is 60 degrees. This arrangement is spatially more flexible, and may lead to localized increases in energy. Meanwhile, molecular dynamics simulations suggest that the rotation of molecular chains is enhanced with the increasing temperature, so the *gauche* conformation, with its greater degree of rotational freedom, emerges more frequently.[49] It should be

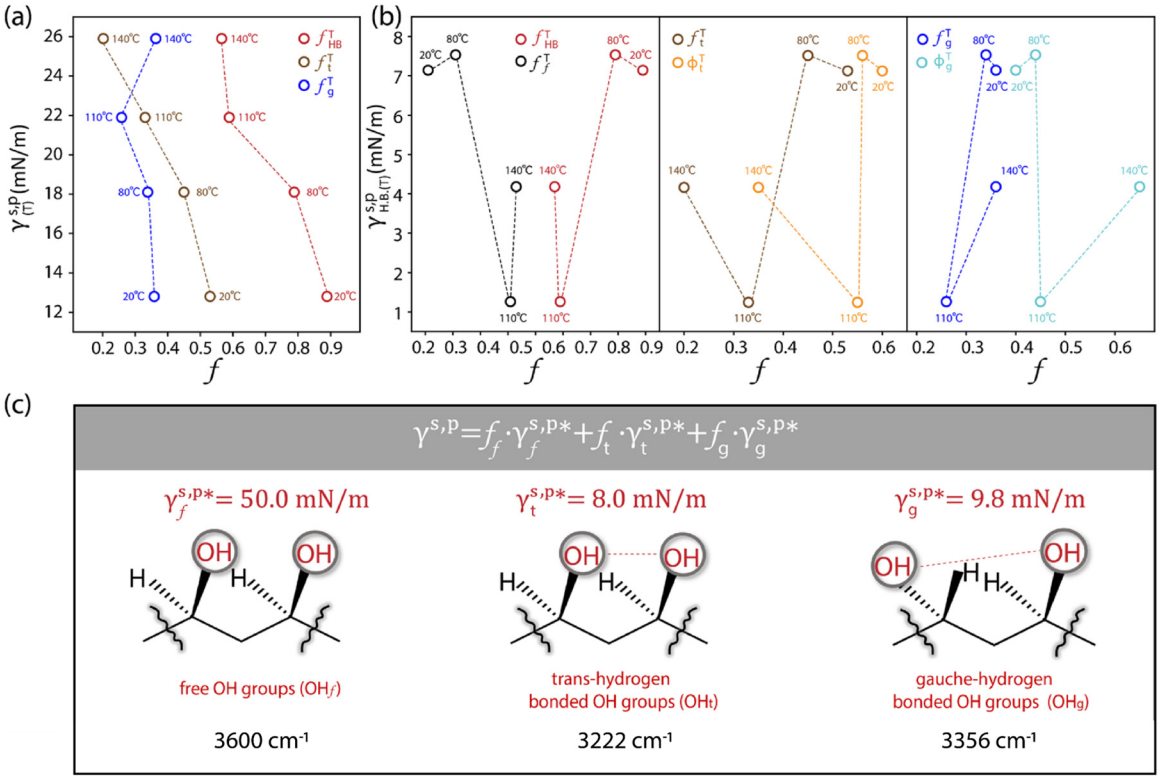

Fig. 3 (a) Plots of the $\gamma^{s,p}_{(T)}$ values of the as-prepared L_PVA$_2^T$ thin films *versus* their f^T_{HB}, f^T_t, and f^T_g values. (b) Plots of the $\gamma^{s,p}_{HB(T)}$ values of the as-prepared L_PVA$_2^T$ thin films *versus* their f^T_{HB} (f^T_f) (left panel), f^T_t (ϕ^T_t) (middle panel), and f^T_g (ϕ^T_g) values (right panel). (c) Schematic summarizing the molecular configurations of the surface OH_f, OH_g, and OH_t groups, with the corresponding $\gamma^{s,p*}_f$, $\gamma^{s,p*}_g$, and $\gamma^{s,p*}_t$ values marked.

noted that the resulting $\gamma^{s,p*}_t$ and $\gamma^{s,p*}_g$ values are more than 5 times smaller than the $\gamma^{s,p*}_f$ of the surface OH_f groups (50 mN m^{-1}), and fairly comparable to the $\gamma^{s,p*}$ values of the weakly polar groups such as Br and pyrrole.[17] Since the majority of OH groups are present on their hydrogen-bonded configurations (for instance, 89% for the L_PVA$_2^{20}$ thin films), these surprisingly weak interactions of the surface OH_{HB} groups with water molecules provide a sensible rationale behind the moderate water wettability of the as-prepared PVA thin films.

3.4 Extension of the developed thermodynamic framework to other PVA thin films

It is important to note that the $\gamma^{s,p*}_t$ and $\gamma^{s,p*}_g$, obtained in Section 3.3, are the intrinsic contributions of the surface OH_t and OH_g groups to the $\gamma^{s,p}$ of the PVA thin films, which should be independent of the methods used to fabricate the PVA thin films. In this scenario, the developed eqn (1) should serve as a thermodynamic framework to rationalize and describe the water wettability of the PVA thin films according to their molecular configurations of surface OH groups, namely, f^T_{HB} and its f^T_t (ϕ^T_t) and f^T_g (ϕ^T_g) components. To assess the validity and generality of eqn (1) and $\gamma^{s,p*}_t$ and $\gamma^{s,p*}_g$ established above, here we prepared an additional three types of PVA thin film surfaces by using the methods reported in the literature,[34,37,38] which were notably different from that used to form L_PVA$_2^T$ thin films (details described in Section 2.2.1). Compared to the model L_PVA$_2^T$ thin films, the resulting H_PVA$_2^{80}$, L_PVA$_7^{RT}$, and M_PVA$_G^{RT}$ films show fairly similar surface morphology and transparency revealed by means of scanning electron microscopy (SEM) imaging (Fig. 4a) and UV-Vis spectrometric analysis (Fig. 4b). Fig. 4c shows that all these PVA films exhibit moderate surface hydrophilicity with fairly large $\theta_{w/a}$ and small $\gamma^{s,p}$ values. It should be noted that the present $\theta_{w/a}$ values are fairly comparable to those reported in the literature,[34,37,38] highlights the reproducibility of the methods reported therein.

The deconvolution of the ATR-FTIR spectra of these PVA thin films *via* Gaussian curve fitting (R^2 of 0.99) reveals that their surface OH groups tend to form hydrogen bonds with each other (Fig. 4d). In the case of the H_PVA$_2^{80}$ thin films, as shown in Fig. 4e, nearly all their surface OH groups are hydrogen bonded together. The f_{HB} is as high as 0.96 with f_t of 0.50 and f_g of 0.46, which are responsible for their $\gamma^{s,p}$ of 10.3 mN m^{-1}. This value is surprisingly low for hydrophilic polymer thin films. In the case of the thin films made of L-PVA, the slight difference in $\theta_{w/a}$ and $\gamma^{s,p}$ between the L_PVA$_2^{20}$ and L_PVA$_7^{RT}$ thin films can be reasonably assigned to the subtle variation in their f_{HB}, f_t, and f_g values. For the M_PVA$_G^{RT}$ thin films, their $\gamma^{s,p}$ is approximately 30.9 mN m^{-1} – 61.8% of the $\gamma^{s,p*}_f$ of the surface OH_f groups – and their f_{HB} is approx. 0.46 with f_t of 0.25 and f_g of 0.21. This highlights that even for the PVA hydrogel films, drying in air can drive a noticeable amount of the OH groups of the PVA chains to form hydrogen bonds together in order to significantly lower the $\gamma^{s,p}$ of the

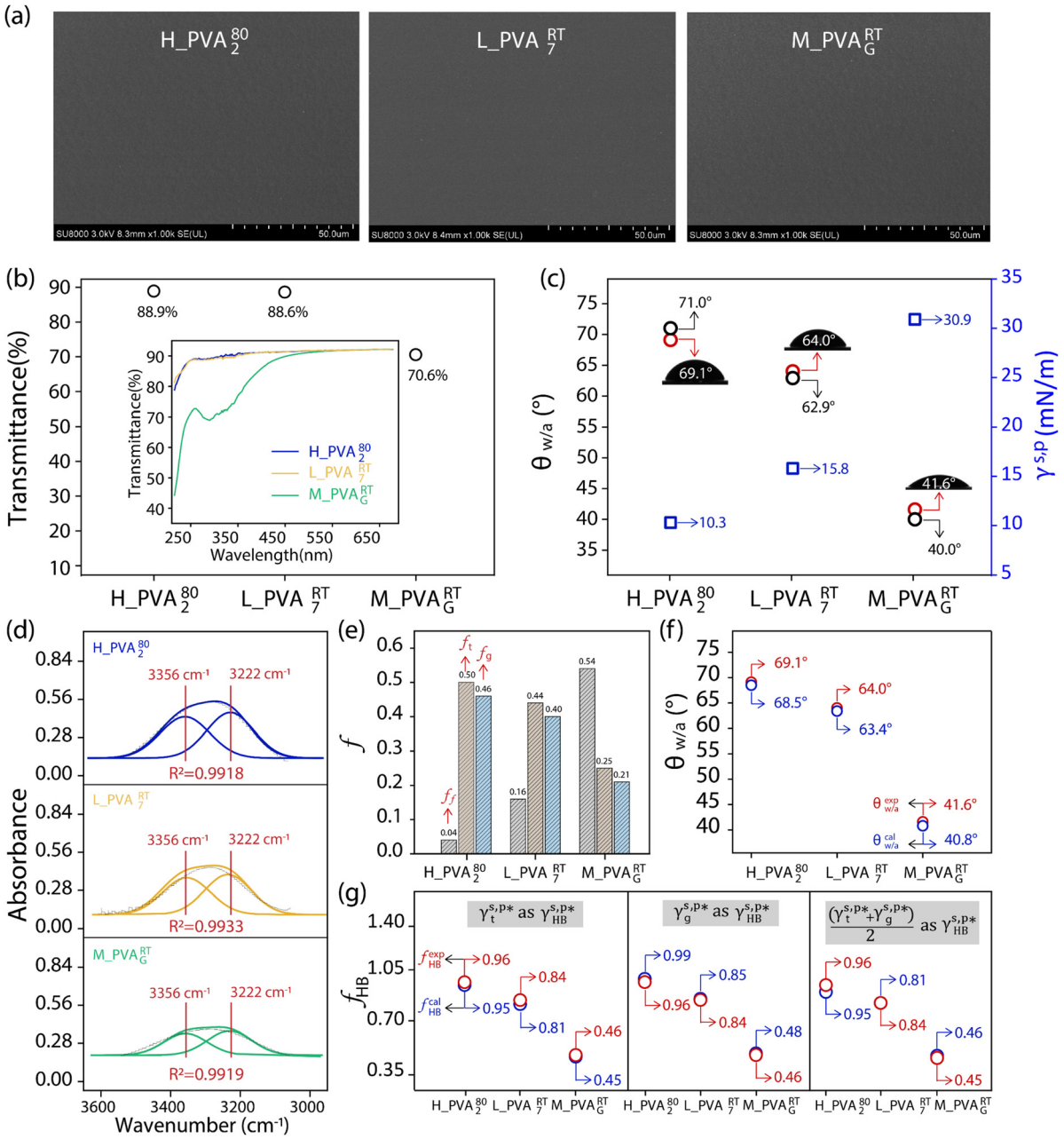

Fig. 4 (a) SEM image of the as-prepared H_PVA$_2^{80}$, L_PVA$_7^{RT}$, and M_PVA$_G^{RT}$ films. (b) Summary of the transmittance values of the resulting H_PVA$_2^{80}$, L_PVA$_7^{RT}$, and M_PVA$_G^{RT}$ films, with the corresponding UV-Vis spectra in the wavelength range of 200–700 nm shown in the inset. (c) Summary of the $\theta_{w/a}$ values of the as-prepared H_PVA$_2^{80}$, L_PVA$_7^{RT}$, and M_PVA$_G^{RT}$ films (red circles), the $\gamma^{s,p}$ values derived from them (blue squares), and the $\theta_{w/a}$ values of the corresponding films reported in the literature (black circles), with schematics of the 2 μL droplets of water placed on the corresponding surfaces shown in the inset. (d) and (e) ATR-FTIR spectra of the OH side groups of the PVA chains of the as-prepared H_PVA$_2^{80}$, L_PVA$_7^{RT}$, and M_PVA$_G^{RT}$ films in the range of 3600–3000 cm^{-1} (d), with the spectra deconvoluted into the vibrational bands of the OH$_t$ and OH$_g$ groups using Gaussian curve fitting, and a summary of their f_f, f_t and f_g values determined from them included (e). (f) Comparison of the $\theta_{w/a}^{cal}$ values (blue circles) of the as-prepared H_PVA$_2^{80}$, L_PVA$_7^{RT}$, and M_PVA$_G^{RT}$ films, derived from their f_{HB}, f_t, f_g values according to eqn (1) and (2), with the corresponding experimentally measured $\theta_{w/a}$ values (red circles) shown in panel c. (g) Summary of the f_{HB}^{cal} values (blue circles) of the as-prepared H_PVA$_2^{80}$, L_PVA$_7^{RT}$, and M_PVA$_G^{RT}$ films, derived from their $\theta_{w/a}$ values using $\gamma_t^{s,p*}$, $\gamma_g^{s,p*}$, and $\frac{\gamma_t^{s,p*}+\gamma_g^{s,p*}}{2}$ as $\gamma_{HB}^{s,p*}$, according to eqn (2) and (13), with the corresponding experimentally measured f_{HB} values shown in panels d and e (red circles).

dried gel films. These results highlight the non-negligible sensitivity of the surface hydrophilicity of PVA thin films on the polymer molecular weight, and the protocols of fabrication or post-treatments of the thin films.

As suggested above, the H_PVA$_2^{80}$, L_PVA$_7^{RT}$, and M_PVA$_G^{RT}$ films are expected to possess $\gamma^{s,d}$ similar to that of the L_PVA$_2^{T}$ thin films (27.1 mN m^{-1}), since it was hardly altered by the experimental conditions. With that in mind, here are the $\gamma^{s,p}$

values of the H_PVA$_2^{80}$, L_PVA$_7^{RT}$, and M_PVA$_G^{RT}$ films were derived from their f_{HB}, f_t, f_g values by using $\gamma_t^{s,p*}$ of 8.0 mN m^{-1} and $\gamma_g^{s,p*}$ of 9.8 mN m^{-1} according to eqn (1), which, subsequently, were utilized to calculate their $\theta_{w/a}$ values – denoted as $\theta_{w/a}^{cal}$ – according to eqn (2). Fig. 4f shows that the $\theta_{w/a}^{cal}$ values of the H_PVA$_2^{80}$, L_PVA$_7^{RT}$, and M_PVA$_G^{RT}$ films are fairly comparable to those experimentally measured with a deviation of less than 2%. In reverse, the use of $\gamma_t^{s,p*}$ and $\gamma_g^{s,p*}$ may also enable us to derive the f_{HB}, f_t, and f_g values of the H_PVA$_2^{80}$, L_PVA$_7^{RT}$, and M_PVA$_G^{RT}$ films from their $\theta_{w/a}$ values (their $\gamma^{s,p}$ values, narrowly speaking) according to eqn (1). For a specific type of PVA thin films, unfortunately, the $\theta_{w/a}$ alone was not sufficient to solve the first-order three-variable function of eqn (1). Instead of determining the f_t and f_g components, here the f_{HB} values of the H_PVA$_2^{80}$, L_PVA$_7^{RT}$, and M_PVA$_G^{RT}$ films – donated as f_{HB}^{cal} – were calculated by utilizing $\gamma_t^{s,p*}$, $\gamma_g^{s,p*}$ or their average $\left(\frac{\gamma_t^{s,p*}+\gamma_g^{s,p*}}{2}\right)$ to serve as the hypothetically intrinsic $\gamma_{HB}^{s,p}$ of surface OH_{OH} groups $\left(\gamma_{HB}^{s,p*}\right)$ according to the variant of eqn (1) or (11):

$$\gamma^{s,p} = (1 - f_{HB}) \cdot \gamma_f^{s,p*} + f_{HB} \cdot \gamma_{HB}^{s,p,*} \quad (14)$$

Fig. 4g shows that the f_{HB}^{cal} values derived from the $\theta_{w/a}$ values of the H_PVA$_2^{80}$, L_PVA$_7^{RT}$, and M_PVA$_G^{RT}$ films are fairly close to those values, experimentally determined by means of ATR-FTIR spectroscopic analysis (Fig. 4e), and the deviation of the f_{HB}^{cal} values obtained by using either $\gamma_t^{s,p*}$ or $\gamma_g^{s,p*}$ as $\gamma_{HB}^{s,p,*}$ from their corresponding experimental values can be as small as 3%. These results confirm the validity and generality of $\gamma_t^{s,p*}$ (8.0 mN m^{-1}), $\gamma_g^{s,p*}$ (9.8 mN m^{-1}), and eqn (1) for the rationalization and description of water wettability on PVA surfaces.

4 Conclusions

In summary, we have managed to quantitatively assess and differentiate the impact of hydrogen bonding configurations of surface OH groups on the surface hydrophilicity of PVA thin films, especially with the assistance of ATR-FTIR spectroscopic analysis. In turn, we can then describe the $\gamma^{s,p}$ of PVA thin films as a sum of the $\gamma_f^{s,p*}$, $\gamma_t^{s,p*}$, and $\gamma_g^{s,p*}$ of the surface OH_f, OH_t and OH_g groups, weighted by the corresponding f_f, f_t, and f_g (eqn (1)). This enabled us to predict the surface hydrophilicity ($\theta_{w/a}$) of the PVA thin films from the molecular hydrogen bonding configurations of their surface OH groups; namely, f_{HB} and its f_t and f_g components or *vice versa* with an accuracy of >97%.

The $\gamma_t^{s,p*}$ and $\gamma_g^{s,p*}$ of the PVA thin films are determined to be 8.0 mN m^{-1} and 9.8 mN m^{-1}, which are more than 5 times smaller than the $\gamma_f^{s,p*}$ of the surface OH_f groups (50 mN m^{-1}) and comparable to that of weak polar groups, thus highlighting the surprisingly weak interactions of the OH_{HB} groups with water molecules. This impact of hydrogen bonding on hydration may be generally expected for polar groups, such as OH, NH_2 and COOH groups bearing both proton acceptors and donors. On the one hand, it is unfavourable for hydrophilic coatings to achieve peculiar surface functionality such as anti-fog, where effective surface hydration is essential to promote aggressive water wetting.[50] On the other hand, it is favourable for hydrogels, where robust hydrogen bonding is necessary to enhance the mechanical strength.[51] Taken together, the present work may offer a technical framework to thermodynamically differentiate the hydrogen bonding of polar groups with themselves from that with water molecules, which will serve as a quantitative guidance to describe and design not only the surface hydration efficiency and water wettability of hydrophilic polymer surfaces, but also the self-organization behaviour of hydrophilic polymers in water.

Author contributions

Z. G.: writing – original draft, methodology, investigation. Z. M.: writing – review & editing, investigation, formal analysis, supervision. D. W.: writing – review & editing, supervision, project administration, funding acquisition, formal analysis, conceptualization. All authors have approved the final version of the manuscript.

Data availability

The data supporting this article, including the original SFG spectra, UV-vis spectra, ATR-FTIR spectra, and XPS spectra, original AFM images, and original SEM images, have been included in the ESI.†

Conflicts of interest

There are no conflicts to declare.

Acknowledgements

This research is funded by the National Natural Science Foundation of China (grant no. 21932003 and 22161132009).

References

1 Y. Q. Xia, V. Adibnia, R. Huang, F. Murschel, J. Faivre, G. J. Xie, M. Olszewski, G. De Crescenzo, W. Qi, Z. M. He, R. X. Su, K. Matyjaszewski and X. Banquy, *Angew. Chem., Int. Ed.*, 2019, **131**, 1322–1328.
2 A. B. Asha, Y. J. Chen and R. Narain, *Chem. Rev.*, 2021, **50**, 11668–11683.
3 D. Hetemi and J. Pinson, *Chem. Rev.*, 2017, **46**, 5701–5713.
4 S. F. Zhao and J. H. Ahn, *Mater. Sci. Eng., R*, 2022, **148**, 100672.
5 A. Abbas, C. Zhang, M. Asad, A. Waqas, A. Khatoon, S. Hussain and S. H. Mir, *Polymers*, 2022, **14**, 238.
6 K. Chaudhuri and J. T. Pham, *Soft Matter*, 2022, **18**, 3698–3704.

7 M. S. Ganewatta, Z. Wang and C. Tang, *Nat. Rev. Chem.*, 2021, **5**, 753–772.
8 Q. Tao, S. Huang, X. Li, X. F. Chu, X. L. Lu and D. Y. Wang, *Angew. Chem., Int. Ed.*, 2020, **59**, 14466.
9 R. Wang, C. L. Cheng, H. Y. Wang, Q. Tao and D. Y. Wang, *Adv. Funct. Mater.*, 2023, **33**, 2301085.
10 Y. X. Zhu, G. R. Guo, J. C. Lu, C. S. Ye, Y. Q. Xie, Y. H. Lu and S. Tu, *Chem. Eng. J.*, 2024, **496**, 153773.
11 S. Huang and D. Y. Wang, *Angew. Chem., Int. Ed.*, 2017, **56**, 1–6.
12 X. Su, D. Z. Hao, Z. N. Li, X. L. Guo and L. Jiang, *J. Mater. Chem. B*, 2019, **7**, 1322–1332.
13 S. Chernyy, M. Järn, K. Shimizu, A. Swerin, S. U. Pedersen, K. Daasbjerg, L. Makkonen, P. Claesson and J. Iruthayaraj, *ACS Appl. Mater. Interfaces*, 2014, **6**, 6487.
14 S. H. Lee and E. Ruckenstein, *J. Colloid Interface Sci.*, 1987, **120**, 529.
15 P. Guo, Y. S. Tu, J. R. Yang, C. L. Wang, N. Sheng and H. P. Fang, *Phys. Rev. Lett.*, 2015, **115**, 186101.
16 T. Sun, G. Wang, L. Feng, B. Liu, Y. Ma, L. Jiang and D. Zhu, *Angew. Chem., Int. Ed.*, 2004, **43**, 357–360.
17 Z. Y. Ma and D. Y. Wang, *Colloids Surf., A*, 2023, **675**, 132031.
18 X. K. Liu, C. L. Leng, L. Yu, K. He, L. J. Brown, Z. Chen, J. Cho and D. Y. Wang, *Angew. Chem., Int. Ed.*, 2015, **54**, 4851–4856.
19 Z. Y. Ma, C. L. Cheng, Q. H. Cheng, R. Wang, Z. H. Guo and D. Y. Wang, *Colloids Surf., A*, 2024, **694**, 134108.
20 M. Kozlov and T. J. McCarthy, *Langmuir*, 2004, **20**, 9170–9176.
21 N. B. Halima, *RSC Adv.*, 2016, **6**, 39823–39832.
22 H. K. Chang, C. W. Huang, C. C. Chiu, H. J. Wang and P. Y. Chen, *Macromolecules*, 2020, **53**, 8809–8818.
23 Y. Liu, J. Y. Yin, Y. B. Fu, P. P. Zhao, Y. H. Zhang, B. Q. He and P. X. He, *Chem. Eng. J.*, 2020, **382**, 122925.
24 J. B. Fan, Y. Y. Song, S. T. Wang, J. X. Meng, G. Yang, X. L. Guo, L. Feng and L. Jiang, *Adv. Funct. Mater.*, 2015, **25**, 5368–5375.
25 Z. X. Bai, K. Jia, C. C. Liu, L. L. Wang, G. Lin, Y. M. Huang, S. N. Liu and X. B. Liu, *Adv. Funct. Mater.*, 2021, **31**, 2104701.
26 J. Lin, Z. Yao, M. M. Xiong, F. Hu, X. C. Wei and S. Y. Huang, *Adv. Compos. Hybrid Mater.*, 2023, **6**, 193.
27 Q. He, Y. Zhong, J. W. Li, S. M. Chai, Y. Q. Yang, S. Q. Liang, Z. Chang, G. Z. Fang and A. Q. Pan, *Adv. Energy Mater.*, 2024, **14**, 2400170.
28 Y. G. Wu, C. H. Xue, X. J. Guo, M. C. Huang, H. D. Wang, C. Q. Ma, X. Wang and Z. Y. Shao, *Chem. Eng. J.*, 2023, **471**, 144313.
29 C. Huang, M. T. Fu, L. Ma, C. K. Mao, Y. Y. Yao, X. Xu, L. Xu, J. G. Han, X. G. Xue, G. Xu, M. H. Wu, H. Y. Shao and H. J. Ma, *Chem. Eng. J.*, 2023, **474**, 145718.
30 H. Lee, M. L. Alcaraz, M. F. Rubner and R. E. Cohen, *ACS Nano*, 2013, **7**, 2172–2185.
31 H. Q. Zou, X. T. Meng, X. Zhao and J. S. Qiu, *Adv. Mater.*, 2023, **35**, 2207262.
32 Y. J. Gu, J. H. Yang and S. X. Zhou, *J. Mater. Chem. A*, 2017, **5**, 10866–10875.
33 W. Zhang, Z. N. Zhang and X. P. Wang, *J. Colloid Interface Sci.*, 2009, **333**, 346–353.
34 W. Zhang, Y. J. Fang and X. P. Wang, *J. Membr. Sci.*, 2007, **303**, 173–182.
35 M. C. Popescu, *Int. J. Biol. Macromol.*, 2017, **101**, 783–790.
36 B. Zuo, Y. Y. Hu, X. L. Lu, S. X. Zhang, H. Fan and X. P. Wang, *J. Phys. Chem. C*, 2013, **117**, 3396–3406.
37 R. Paneru, S. H. Ki, P. Lamichhane, L. N. Nguyen, B. C. Adhikari, I. J. Jeong, S. Mumtaz, J. Choi, J. S. Kwon and E. H. Choi, *Appl. Surf. Sci.*, 2020, **532**, 147339.
38 Y. Liu, H. Y. Hu, X. L. Yang, J. Lv, L. Zhou and Z. K. Luo, *Biomed. Mater.*, 2019, **14**, 055009.
39 M. Fowkes, *J. Ind. Eng. Chem.*, 1960, **12**, 40–52.
40 S. W. Wu, M. T. Hua, Y. Alsaid, Y. J. Du, Y. F. Ma, Y. S. Zhao, C. Y. Lo, C. R. Wang, D. Wu, B. W. Yao, J. Strzalka, H. Zhou, X. Y. Zhu and X. M. He, *Adv. Mater.*, 2021, **33**, 2007829.
41 R. Kurapati and U. Natarajan, *Ind. Eng. Chem. Res.*, 2020, **59**, 16099–16111.
42 K. Masuda and F. Horii, *Macromolecules*, 1998, **31**, 5810.
43 K. Masuda, H. Kaji and F. Horii, *J. Polym. Sci., Polym. Phys. Ed.*, 2000, **38**, 1.
44 G. M. Whitesides, P. E. Laibinis and J. P. Folkers, *Langmuir*, 1992, **8**, 1330–1341.
45 S. Han, Y. M. Luan, S. F. Pang and Y. H. Zhang, *Spectrochim. Acta, Part A*, 2015, **139**, 37–42.
46 E. G. Kononova, M. N. Rodnikova, I. A. Solonina and E. V. Shirokova, *Russ. J. Phys. Chem. A*, 2020, **94**, 2233–2237.
47 S. Hassen, H. Chebbi, M. F. Zid and Y. Arfaoui, *J. Mol. Struct.*, 2019, **1179**, 678–684.
48 Z. Z. Fu, S. J. Guo, C. X. Li, K. Wang, Q. Zhang and Q. Fu, *Phys. Chem. Chem. Phys.*, 2022, **24**, 1885–1895.
49 P. Pruettiangkura, S. Ho and M. Schwartz, *Spectrosc. Lett.*, 1979, **12**, 679–685.
50 H. Lee, M. L. Alcaraz, M. F. Rubner and R. E. Cohen, *ACS Nano*, 2013, **3**, 2172–2185.
51 S. Wu, M. Hua, Y. Alsaid, Y. Du, Y. Ma, Y. Zhao, C. Lo, C. Wang, D. Wu, B. Yao, J. Strzalka, H. Zhou, X. Zhu and X. He, *Adv. Mater.*, 2021, **33**, 2007829.